Winter 12-1-2014

Slow Strain Rate Testing and Stress Corrosion Cracking of Ultra-Fine Grained and Conventional Al–Mg Alloy

Mala M. Sharma
Bucknell University

Josh D. Tomedi
Bucknell University

Timothy J. Weigley
Bucknell University

Materials Science & Engineering A 619 (2014) 35–46

Contents lists available at ScienceDirect

Materials Science & Engineering A

journal homepage: www.elsevier.com/locate/msea

Slow strain rate testing and stress corrosion cracking of ultra-fine grained and conventional Al–Mg alloy

Mala M. Sharma [a,*], Josh D. Tomedi [a], Timothy J. Weigley [b]

[a] Bucknell University, Department of Mechanical Engineering, Lewisburg, PA 17837, USA
[b] Bucknell University, Department of Civil and Environmental Engineering, Lewisburg, PA 17837, USA

ARTICLE INFO

Article history:
Received 31 July 2014
Received in revised form
12 September 2014
Accepted 12 September 2014
Available online 22 September 2014

Keywords:
Mechanical characterization
Al–Mg alloys
Ultra-fine grain
Slow strain rate testing
Stress corrosion cracking

ABSTRACT

Stress corrosion cracking susceptibility was investigated for an ultra-fine grained (UFG) Al–7.5Mg alloy and a conventional 5083 H111 alloy in natural seawater using slow strain rate testing (SSRT) at very slow strain rates between $1E^{-5}\,s^{-1}$, $1E^{-6}\,s^{-1}$ and $1E^{-7}\,s^{-1}$. The UFG Al–7.5Mg alloy was produced by cryomilling, while the 5083 H111 alloy is considered as a wrought manufactured product. The response of tensile properties to strain rate was analyzed and compared. Negative strain rate sensitivity was observed for both materials in terms of the elongation to failure. However, the UFG alloy displayed strain rate sensitivity in relation to strength while the conventional alloy was relatively strain rate insensitive. The mechanical behavior of the conventional 5083 alloy was attributed to dynamic strain aging (DSA) and delayed pit propagation while the performance of the UFG alloy was related to a diffusion-mediated stress relaxation mechanism that successfully delayed crack initiation events, counteracted by exfoliation and pitting which enhanced crack initiation.

1. Introduction

The mechanical properties of aluminum–magnesium alloys as a function of strain rate are of interest in regard to how stress corrosion cracking affects ultra-fine grain materials used in structural applications. Conventionally processed aluminum–magnesium alloys possess excellent corrosion resistance compared to many other aluminum alloys [1–4]. Precise control of the microstructure during manufacturing allows these alloys to retain many of the properties that make them attractive as structural materials while enhancing the strength to weight ratio of the material. Furthermore, by decreasing grain size, an increase in ultimate strength can be achieved [5]. But there is conflicting data on the reported trends of the mechanical properties for nanocrystalline (NC) and UFG materials as a function of strain rate and environment [6–9]. The study of these properties and the related trends is important to understanding the mechanism(s) behind the material behavior. Al 5083 is a non-heat treatable, predominately aluminum–magnesium based alloy that is often used in marine and naval applications and could benefit from improved strength and corrosion resistance. Researchers have made numerous attempts to manufacture fine particles that maintain their grain size after consolidation [10–12]. Cryomiling involves ball milling metal materials with liquid nitrogen, breaking apart by particles through brittle fracture to form nano-sized powder particles [13]. Upon consolidation, some particles combine and grow while others maintain their original size to form an ultra-fine grained microstructure. Cryomilling has several advantages over other manufacturing techniques including intense grain refinement, reduced oxygen contamination and limited heat generation [13], so recrystallization and significant grain growth does not occur.

Pitting corrosion is a primary damage mechanism affecting aluminum materials used in marine environments. Most aluminum alloys naturally create a thin oxide layer on the surface of the alloy that acts as a protective layer, reducing the corrosion rate. However, when an imperfection in the layer is created, often through normal service conditions or damage to a structure, localized pitting corrosion initiates and promotes accelerated dissolution of the surrounding metal. Second-phase particle induced pitting corrosion in aluminum alloys has been studied by utilizing microscopy techniques such as optical and scanning electron microscopy (SEM) with energy dispersive spectroscopy (EDS). The objective of these investigations was to identify the contribution of pitting corrosion in relation stress corrosion cracking [14,15].

For the most part, it has been concluded that both anodic dissolution and some form of hydrogen embrittlement are the major mechanisms causing and intensifying stress corrosion cracking [2,16–18]. As grain size is decreased or varied for the

* Corresponding author. Tel.: +1 570577 1686; fax: +1 5705777281.
E-mail address: mala.sharma@bucknell.edu (M.M. Sharma).

http://dx.doi.org/10.1016/j.msea.2014.09.062
0921-5093/

Al–Mg alloy, susceptibility of SCC has been found to increase [16] and decrease [1,2], with variables such as type of applied stress, exposure environment and composition of the alloy having an effect on the outcome. Researchers have found that varying strain rate has an effect on the mechanical properties of Al-5083, particularly the magnitude of the percent elongation as well as the ultimate and failure stresses [19–21]. The ultimate tensile stress of conventional Al–Mg alloys have been reported to be between 450 and 500 MPa while cryomilled UFG Al–Mg alloys sustain stresses upwards of 700–750 MPa [8,20]. Negative and positive strain rate sensitivity in air has been reported for NC and UFG alloys [20,22–25]. The sensitivity to strain rate at exceedingly low strain rates has yet to be investigated in a corrosive environment and compared across conventional and UFG Al–Mg alloys. If NC or UFG Al–Mg alloys are to be accepted as viable for naval and structural applications, the sensitivity to SCC as a function of strain rate should be foreseeable and comparable to current conventional Al–Mg alloys. The objective of this study is to compare the mechanical performance of conventional and UFG 5083 as a function of strain rate in a natural seawater environment in order to identify the mechanisms behind the resulting performance.

2. Experimental

2.1. Materials

In an effort to compare the SCC behavior as a function of strain it is necessary to choose two materials, one representing the current conventional process alloy and the other, a cryomilled UFG alloy. These same materials have been the focus of a larger study involving the investigation of the corrosion resistance of NC and UFG alloys [1,2,17]. The materials chosen are a conventionally processed 5083-H111 alloy and an ultra-fine grained (UFG) partially nanocrystalline (NC) Al–7.5Mg alloy. The aluminum alloy 5083-H111 can be classified as a wrought alloy product and was chosen because it is used for a variety of marine applications due to its excellent corrosion resistance. Although the compositions between the two alloys are slightly different, the temper of the conventional alloy closely matches the manufacturing process of the UFG alloy. The compositions of the Al 5083-H111 and UFG Al–Mg alloys, in weight percent, are given in Table 1. The UFG Al–7.5Mg alloy was manufactured by the Boeing Company in collaboration with the University of California, Irvine. The material was processed through a series of steps involving cryomilling and subsequent hot pressing. The details of the process can be found in previously published work [1,2,17].

2.2. Specimen design and testing

Specimens measuring 101 mm long and 6.35 mm in diameter were utilized in the slow strain rate testing and are shown in Fig. 1. In order to prepare the samples, round bars were EDM'd (electro-discharge machined) from the main extrusion and then machined to the final dimensions. Slow strain rate tests were conducted at the LaQue Center for Corrosion Technology (LCCT) in Wrightsville Beach, North Carolina. To test the specimen, an MTS 810 servo hydraulic system was employed using a Model 490 digital controller and Test Star software. Samples were tested in triplicate at strain rates of $1E^{-5}$, $1E^{-6}$ and $1E^{-7}$ s^{-1} until failure in a natural seawater environment. The seawater was pumped in from the ocean assuring fresh electrolyte was in constant contact with the

Table 1
Alloy compositions in weight percent.

	5083-H111	UFG Al–7.5Mg
Mg	4–4.9	7.5
Fe	< 0.4	0.09
Cr	0.05–0.25	–
Mn	0.4–1.0	–

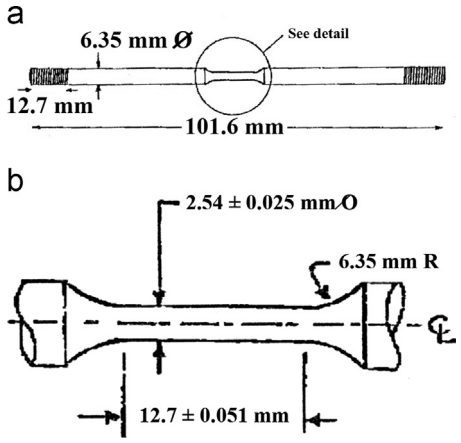

Fig. 1. Dimensions of the SSRT specimen; the entire specimen is shown in (a), while (b) shows the close up of gauge section.

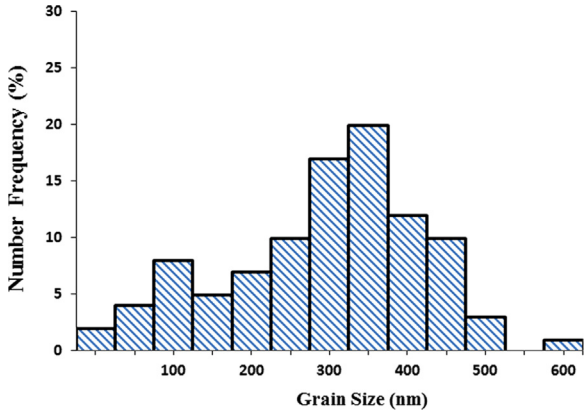

Fig. 2. Grain size distribution of UFG Al–7.5Mg alloy.

Table 2
Summary table of SSRT results.

Alloy	Strain rate [s^{-1}]	Elastic limit [MPa]	R.A. [%]	Elong [%]	YS [MPa]	UTS [MPa]	Fracture energy [J/m^3]
5083H111	1.00E−05	178	17.2	14.1	181.0	309.1	34.1
		184	20.6	15.2	183.7	314.6	38.1
		169	22.6	14.9	190.3	312.8	36.2
	1.00E−06	177	13.4	16.5	194.0	316.3	41.7
		179	17.0	17.2	190.0	318.3	42.4
		177	16.9	17.0	189.0	317.3	42.1
	1.00E−07	168	15.4	18.9	191.1	316.4	38.1
		170	15.2	19.3	197.4	320.0	51.6
		170	13.5	19.8	194.9	324.2	52.6
UFG Al–7.5Mg	1.00E−05	444	27.8	12.2	500.9	519.3	47.7
		482	27.8	14.0	527.2	539.2	53.6
		459	29.4	13.3	504.5	527.1	51.4
	1.00E−06	470	26.0	13.1	519.8	529.5	51.0
		454	29.5	15.2	520.6	520.4	55.6
		449	37.6	14.5	530.0	535.9	56.4
	1.00E−07	408	36.0	16.7	489.9	508.8	64.2
		409	36.8	17.3	478.8	490.7	65.3
		411	36.0	16.9	471.5	487.7	65.6

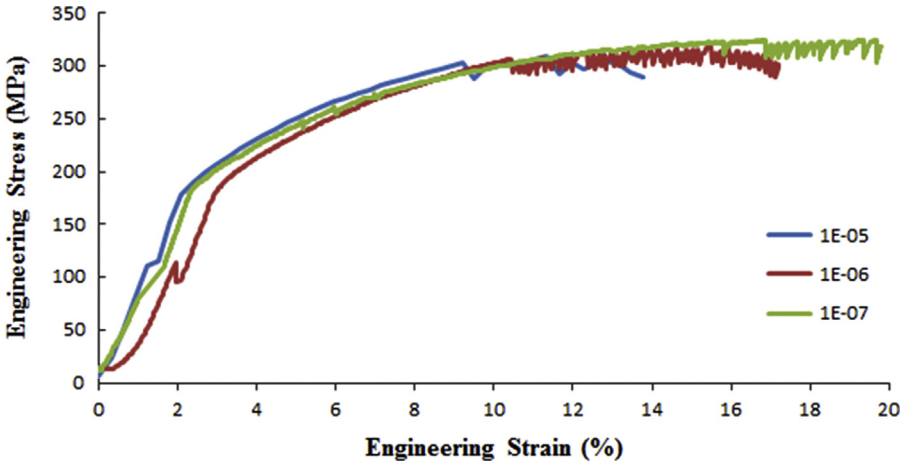

Fig. 3. Engineering stress vs. engineering strain for the conventional 5083H111 alloy tested in natural seawater at various strain rates.

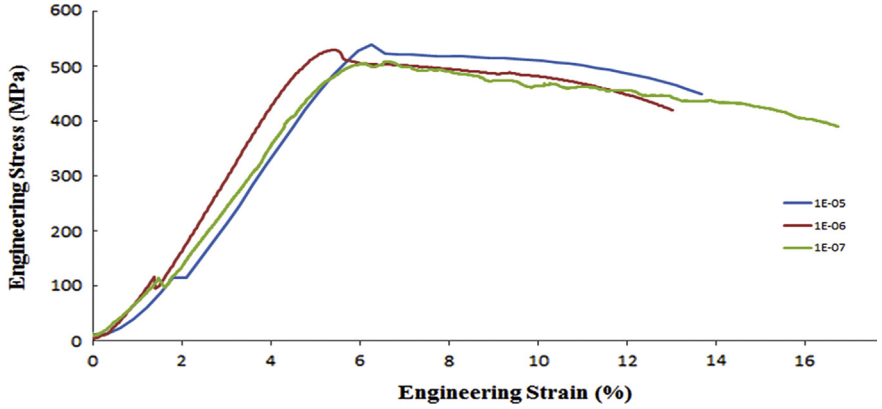

Fig. 4. Engineering stress vs. engineering strain for the UFG Al–7.5Mg alloy tested in natural seawater at various strain rates.

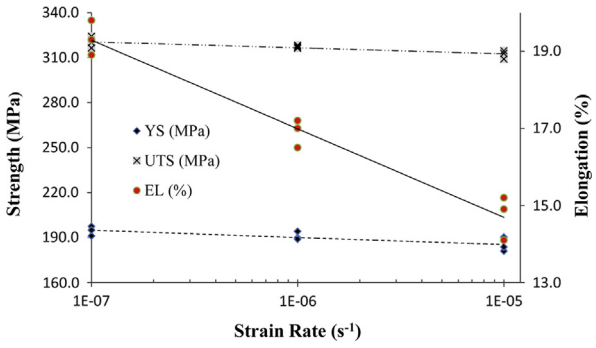

Fig. 5. Conventional 5083 H111 strength and elongation results as a function of strain rate.

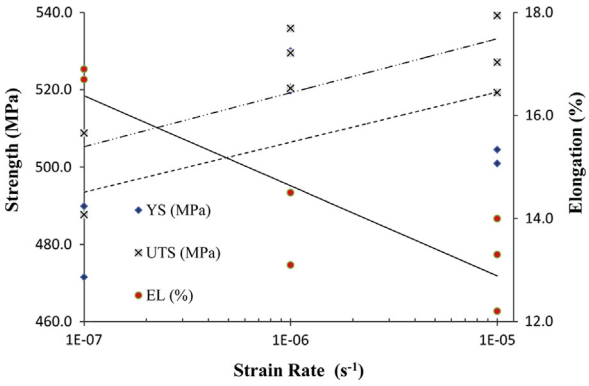

Fig. 6. UFG Al–7.5Mg strength and elongation results as a function of strain rate.

gage section of the specimen; while the rest of the sample remained unexposed to the electrolyte. At failure, the maximum stress, percent elongation and fracture energy were noted for each sample. Furthermore, stress vs. elongation plots were generated for the entire duration of testing for each specimen. After failure, samples were examined using optical and SEM along with EDS.

3. Results

The detailed characterization of the microstructure for the materials in this study is discussed in detail elsewhere [1,2,17]. Previous authors who worked on these same NC/UFG alloys found the average grain size to range between 300 and 500 nm with several grains smaller than 100 nm [1]. We found the particle size varies from approximately 25–500 nm with the distribution frequency as shown in Fig. 2. For this reason, the material in this paper is referred to an ultra-fine grained (UFG) alloy instead of nanocrystalline (NC). These same authors did not note any precipitates or second phases in the TEM micrographs of the UFG alloy. However, they did discover fine precipitates within the grains on the conventional 5083 alloy that were reported to be the secondary β-phase Al_3Mg_2 [1,26]. In recent studies which

investigated the microstructure of similarly processed UFG and NC 5083 materials, four different types of second phase particles were said to be present in these materials and include grain boundary Mg–O oxides, precipitates of $Al_{12}Mg_2(CrMnFe)$ and $Al_{12}(FeMn)_3Si$, particles of $Al_6(CrMnFe)$ and Al–Si–O dispersoids [8,27]. It is believed that these phases are present in some forms within the UFG alloys since the processing method is identical to the previous researchers' materials. Due to the fact that the compositions vary slightly, particle volume fraction and distribution within the current materials is unknown. It is recognized however, that even a small amount of dispersoids contribute to the strengthening and stabilization of the microstructure [8,28,29].

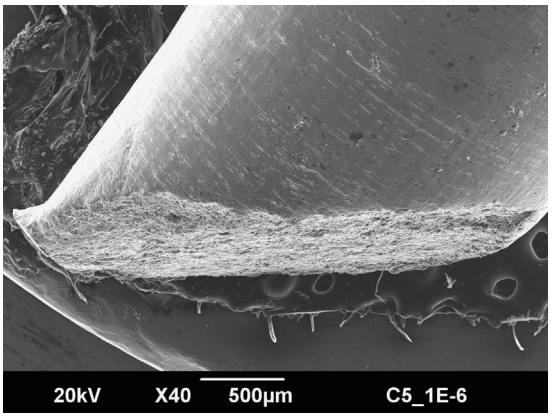

Fig. 7. SEM micrograph showing macroscopic failure morphology of conventional 5083 alloy with shear lip on periphery.

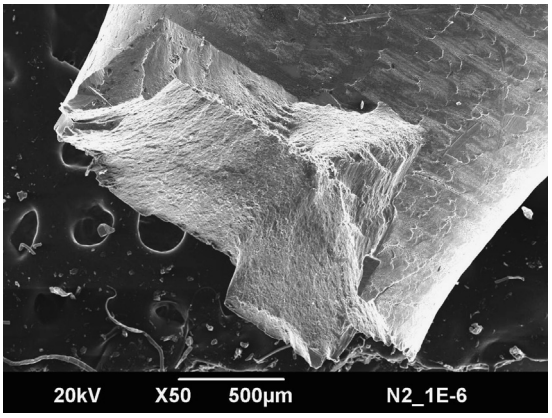

Fig. 8. SEM micrograph showing macroscopic failure morphology of UFG Al–7.5Mg alloy. Brittle fracture can be observed at numerous initiation sites.

Presented in Table 2 are the results of the SSRT for the UFG Al–7.5Mg and conventional 5083 alloy. At the higher strain rates, elongation at failure values for the UFG Al–7.5Mg were between 12% and 14%, while the conventional alloy displayed values between 14% and 15% at the same strain rate. As the strain rate decreased, average elongation values increased for both materials, with UFG Al–7.5Mg alloy reaching almost 17% and the conventional 5083 reaching nearly 20%. Another interesting trend was that the conventional 5083 alloy had a reduction in area which decreased as a function of decreasing strain rate while the opposite was noted for the UFG alloy. The elastic region for the 5083 alloy began to yield at approximately 2.00–2.25% elongation and remained relatively constant as strain rate increased while the UFG Al–7.5Mg alloy began to yield at approximately 4.00–4.25% elongation and increased to approximately 5% as strain rate increased. Both alloys exhibited a “slip” or a “pause” during elastic deformation; this occurred at approximately 115 MPa at each strain rate for each material. It is unknown if this was machine software related or due to a material response.

The representative stress–strain curves for the conventional 5083 conducted in the natural seawater environment are presented in Fig. 3. At all the three strain rates, these curves reveal significant work hardening and deformation, with uniform deformation increasing with decreasing strain rate. For all strain rates, the sample failed shortly after the peak stress was reached. The UFG Al–7.5Mg alloy displayed significantly different behavior than the conventional 5083. Fig. 4 shows representative stress–strain curves for the UFG Al–7.5Mg alloy. Unlike its conventional counterpart, the UFG alloy does not work harden at a slow and steady pace until after yielding and recovery. Similar to the conventional

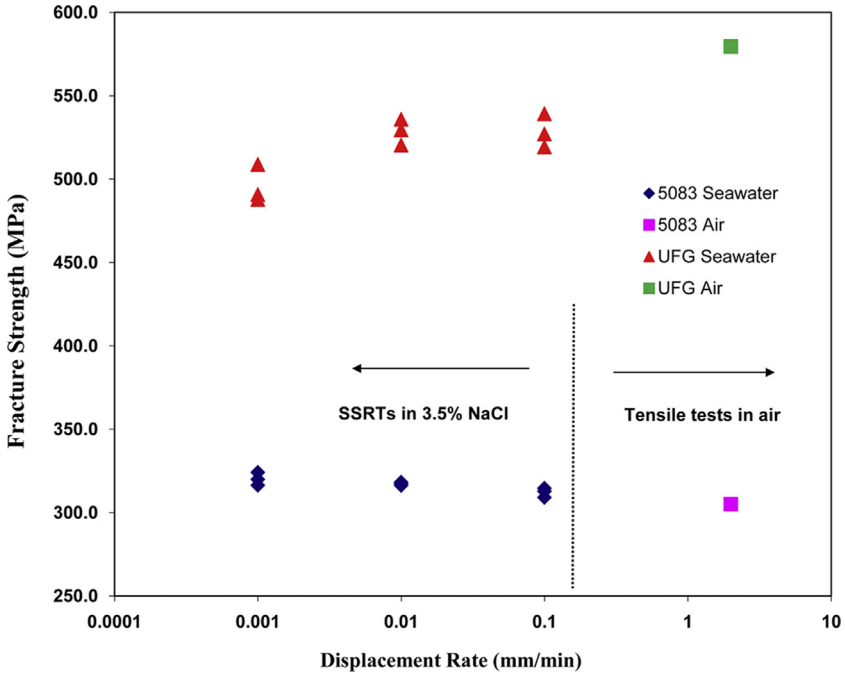

Fig. 9. Fracture strength as a function of displacement rate for both materials.

5083 alloy, deformation increases when the strain rate is decreased and is most pronounced at a strain rate of $E^{-7}\,s^{-1}$.

In order to evaluate the strain rate dependence of strength and elongation in a natural seawater environment, these results were plotted as a function of strain rate, Fig. 5. For the conventional alloys, inspection of the strain rate dependence reveals that as strain rate increases, elongation decreases significantly, while the ultimate tensile strength and yield strength decrease slightly. The conventional alloy had an average ultimate strength of 324 MPa at a strain rate of $E^{-7}\,s^{-1}$ and decreased to 312 MPa at $E^{-5}\,s^{-1}$. For the UFG Al–7.5Mg alloy, Fig. 6, it is interesting to note that similar to the conventional 5083 alloy, it displayed decreasing elongation with increasing strain rate; however, the ultimate tensile strength and yield strength both increase with increasing strain rate. On average, the ultimate tensile strength was 481 MPa at a strain rate of $1E^{-7}$ and increased slightly to an average of 511 MPa at $1E^{-5}$. The amount of energy required to fracture the specimen was greater for the UFG Al-7.5Mg alloy at all strain rates and increased as strain rate decreased. On average, the conventional 5083 alloy fractured at 36 J/m^3 and increased to 50 J/m^3 from the highest to lowest strain rate while the UFG Al–7.5Mg alloy fractured with approximately 51 J/m^3 and increased to 65 J/m^3. The energy required to fracture the specimen in the seawater environment actually increased 38.8% for the conventional alloy and 27.5% for the UFG Al–7.5Mg as strain rate is decreased.

In order to understand the differences in mechanical behavior between the two materials, the fracture surfaces and gage section

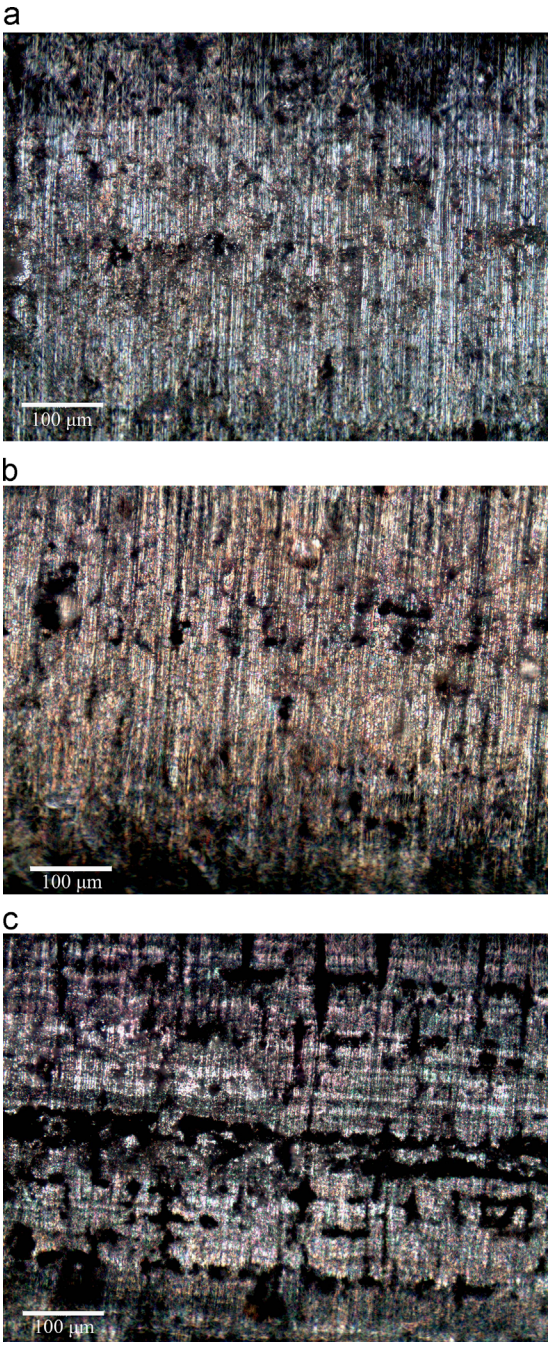

Fig. 10. Optical micrographs showing the progression of corrosive attack as a function of strain rate (a) $E^{-5}\,s^{-1}$, (b) $E^{-6}\,s^{-1}$, and (c) $E^{-7}\,s^{-1}$ for the conventional 5083 H111 alloy.

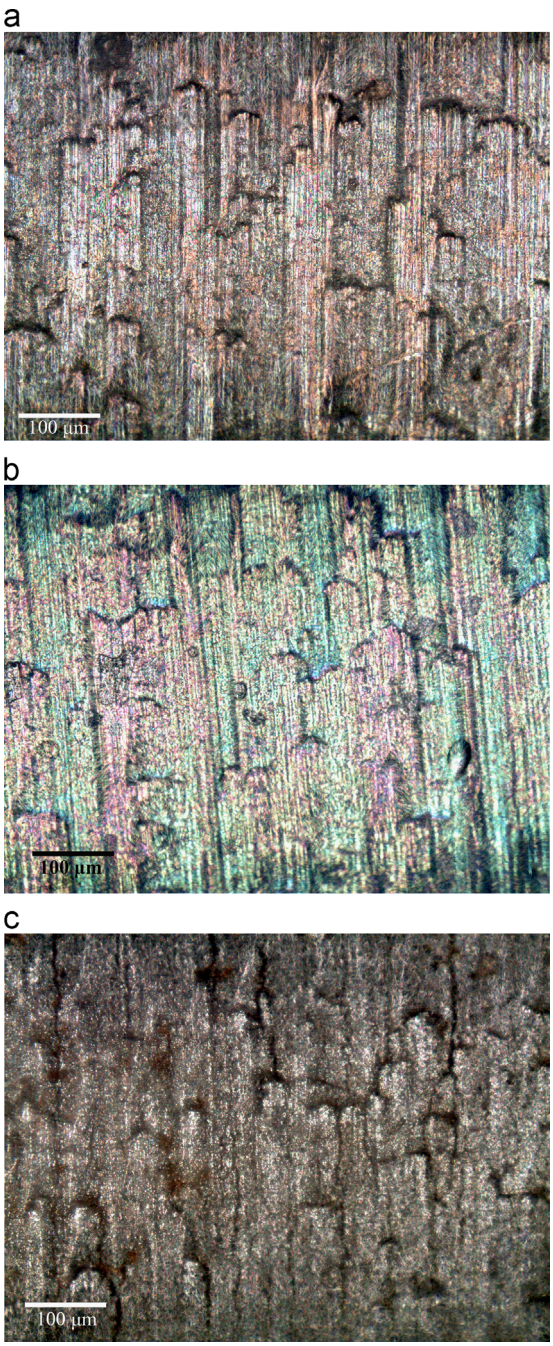

Fig. 11. Optical micrographs showing the corrosive attack as a function of strain rate (a) $E^{-5}\,s^{-1}$, (b) $E^{-6}\,s^{-1}$, and (c) $E^{-7}\,s^{-1}$ for the UFG Al–7.5Mg alloys. Secondary cracking emanating from the exfoliations can be observed.

of each sample was examined by optical and scanning electron microscopy with EDAX. These results are used in the following discussion to explain the behavior of the materials studied.

4. Discussion

The percent elongation values for the UFG Al–7.5Mg specimens were much higher than anticipated and compared well with those of the conventional 5083 alloy, Table 2. It is exceptional that the UFG Al–7.5Mg alloy could display such a high elongation while maintaining a high maximum tensile strength in a corrosive environment. Chang and Chuang [3] investigated the SCC of various superplastically formed 5083 alloys by employing SSRT in 3.5% NaCl solution. Their materials attained higher UTS (251–358 MPa), lower YS (132–164 MPa) and varied elongation values (4.3–7.6% and 24.5–33.6%) when tested at a strain rate of $1E^{-6}\,s^{-1}$. Although the researchers did not provide an exact composition of their materials, it is clear that the manufacturing method alone had an effect on the mechanical performance of their materials. The varied performance of the UFG Al–7.5Mg alloy is believed to be due to compositional dissimilarities as well as grain size variation between the two alloys as a result of manufacturing methods. The improving properties with decreasing grain size has been documented and can be described by the Hall–Petch relationship which relates the strength of the material to be equal to the inverse square root of the grain size [5]. Detailed examination of the stress–strain curves reveals that the flow stress for both alloys increases during plastic deformation, but the conventional 5083 alloys fractured in the work hardened region while the UFG Al–7.5Mg alloy fails after yielding, recovery and subsequent work hardening. This dissimilarity in behavior is indicative of different mechanisms influencing the two materials. This variation in mechanisms is believed to be related to dislocation density. Han et al. [8] investigated the strain rate ductility of cryomilled nanocrystalline Al 5083 (Al–4.2 wt% Mg–0.67 wt% Mn) and observed their samples to fracture in the work hardened region with very little tensile elongation. The stress–strain behavior of their materials was nearly identical under tensile and compressive loading. They attributed the similarity to the same dislocation density mechanism which allowed early strain hardening behavior.

Erratic serrated stress–strain behavior can be observed just before failure and gets increasingly volatile as the strain rate

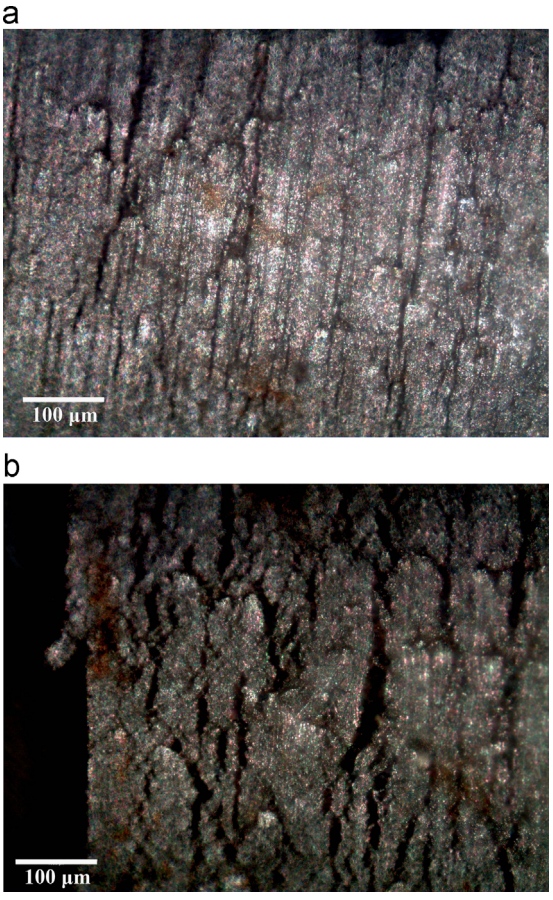

Fig. 12. Optical micrographs showing extensive secondary corrosion cracking at (a) $E^{-5}\,s^{-1}$ and (b) $E^{-6}\,s^{-1}$strain rates for the UFG Al–7.5Mg alloys.

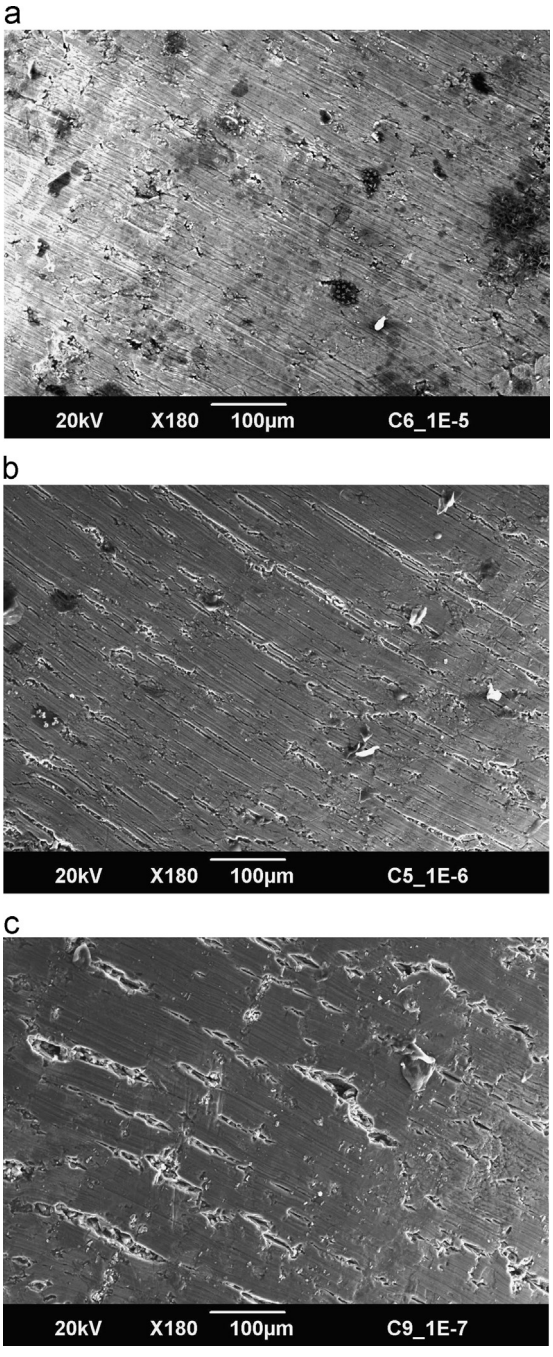

Fig. 13. SEM micrographs of the conventional 5083 showing progression of corrosion damage as a function of strain rate: (a) $E^{-5}\,s^{-1}$, (b) $E^{-6}\,s^{-1}$, and (c) $E^{-7}\,s^{-1}$.

decreases for the conventional alloy, Fig. 4. This inhomogeneous behavior is believed to be caused by the Portevin–Le Chatelier (PLC) effect which is related to dynamic strain aging (DSA) [13,18,19,30,31]. Although the terms are often used interchangeably, DSA is the microscopic mechanism which induces the PLC effect that is related to solid solution strengthening mechanisms and thus creates a negative strain rate response [16]. Investigators have attempted to develop a method to categorize the various serrations which are usually dependent on factors such as temperature, grain size and strain rate [32]. Most prominent in the literature are the bands identified as A, B and C, but researchers have also recognized D and E type bands [32,33] exist. Fig. 3 reveals that the PLC effect takes longer to have an influence as strain rate decreases. Only after smooth strain, ε_c, is displayed does the PLC effect begin, displaying a strong dependence on strain rate. Several researchers have [22,34–37] observed that PLC effect initiates at the yield point for strain rates greater than 5×10^{-4} s^{-1} and below that a pre-strain is required before PLC serrations can be detected. This behavior is compatible with DSA, if dislocation density and additional DSA enthalpy are taken into consideration [22]. Abbadi et al. and Klose et al. [35,36] associated this specific behavior with C type serrated bands at low strain rates and attributed them to nucleation and not propagation.

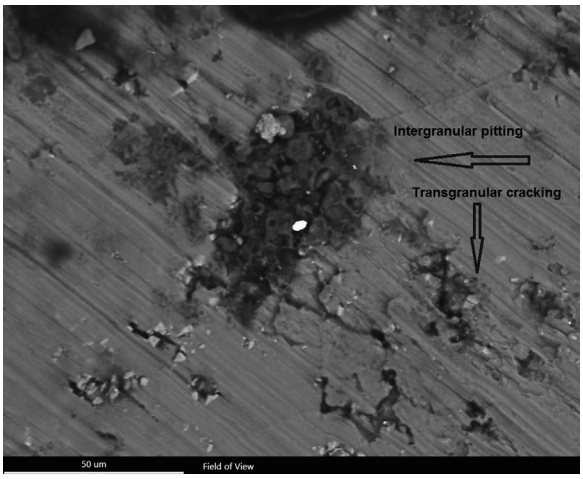

Fig. 14. SEM micrograph for the conventional 5083 showing intergranular corrosion attack in a pit approximately 150 μm in diameter. Secondary transgranular cracking is also present. The sample as tested at a strain rate of E^{-5} s^{-1}.

The serrated PLC stress–strain behavior is not observed in the UFG alloy; at the slowest strain rate $1E^{-7}$ s^{-1} however, there is some evidence of irregular loading response (Fig. 4). This behavior is attributed more to the initiation of corrosive/pitting attack vs. the PLC effect as it was not observed in either of the faster strain rates. In addition to the grain size effect, the UFG Al–7.5Mg alloy has approximately 2.6–3.0 wt% more Mg. Győző Horváth et al. [38] studied the effect of Mg concentration on the plastic deformation behavior of Al–Mg alloys and found the characteristics of Portevin–Le Chatelier plastic instabilities to depend strongly on the Mg concentration. They found that dislocation densities increase with increasing Mg content. Mg atoms have a preferential desire to locate in the stretched region of edge dislocations, whereby the tensile strains surrounding the dislocations are decreased due to obstructed motion [39]. This behavior results in a more even distribution of dislocations dispersed through the dislocation–solute interaction space, thus minimizing the strain energy with higher Mg concentration. However, because there is more Mg in the UFG Al–7.5Mg alloys there is also more intermetallic Mg_2Al_3-β strengthening phase particles which also provide additional sites for corrosion [2]. These particles are sites for the development of anodic corrosion, which actually negates the strengthening contribution from the PLC effect.

Macroscopic examination of the fractured specimen revealed that the conventional 5083H111 aluminum specimen showed some necking and evidence of a shear lip with the fracture typically at a 45° shear (Fig. 7). In contrast, the UFG Al–7.5Mg

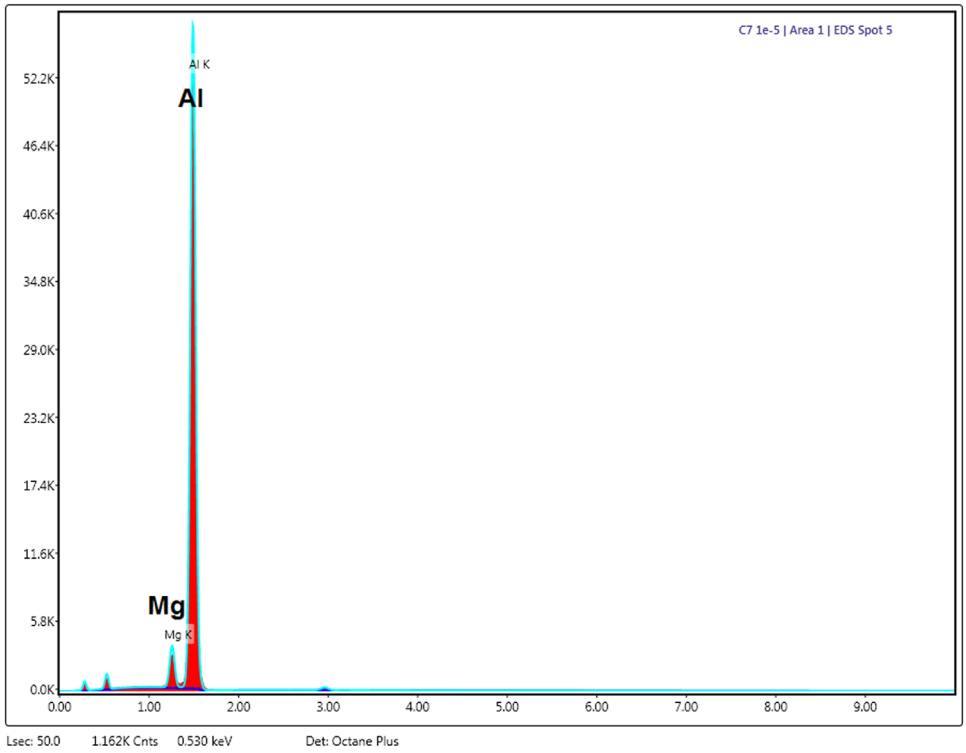

Fig. 15. EDAX pattern showing Al and Mg is present in the corrosion attack on the surface of the conventional 5083 alloy.

alloy displayed signs of multiple failure initiation sites, especially at the lowest strain rate. The fracture did not appear to have typical cup and cone characteristics, but rather had a macroscopic brittle failure appearance with a plateau in the middle of the specimen accompanied by a small shear lip (Fig. 8). The distinction between brittle and ductile macroscopic fractographic features can be attributed to the continuous precipitation of the β phase [2]. This strengthening phase has high active corrosion potential, which leads to pitting from anodic dissolution of the precipitates located at grain boundaries [3,4,18]. The result is accelerated intergranular corrosion and subsequent intergranular fall out of particles from stress corrosion cracking.

In order to investigate the effect of strain rate variation and environment on the strength of the alloys, the fracture strength was plotted as a function of displacement rate and is presented in Fig. 9. The values for tensile testing in air were obtained from previous work [2]. In the UFG Al–7.5Mg alloy at strain rates of $1E^{-5}$, $1E^{-6}\,s^{-1}$ in natural seawater, the fracture strength decreased from the results in air, and more significantly at $1E^{-7}\,s^{-1}$. In the conventional alloy, varying the environment and strain rate did not seem to have as substantial an effect on the fracture strength. Unlike the tensile results executed in air, a crack that caused final failure in natural seawater was typically initiated at the sample surface for the UFG materials at the slowest strain rate.

Microstructure analysis was conducted on the fracture surface to identify the cause(s) and location of failure. Fig. 10(a–c) shows the optical micrographs in the gage section near the failure location for the two alloys after SSRT. The conventional alloys show a steady progression of pit initiation and cracks which start at a strain rate of $1E^{-5}\,s^{-1}$, as strain rate decreases, the pits grow larger and more numerous. At a strain rate of $1E^{-7}\,s^{-1}$, the pits are large enough to eventually coalesce into deep cracks that lead to

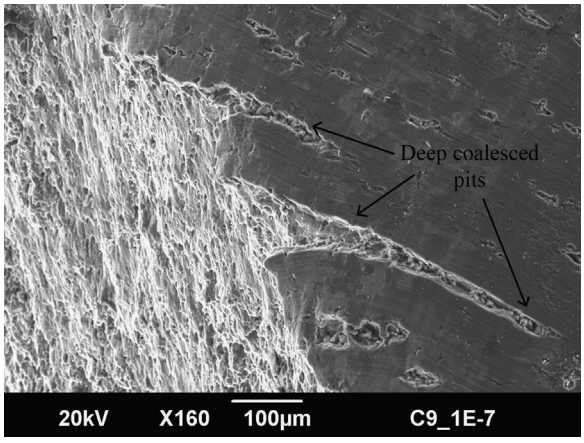

Fig. 18. SEM micrograph showing deep pits which coalesced and led to failure for the conventional 5083 alloy tested at a strain rate of $1E^{-7}\,s^{-1}$.

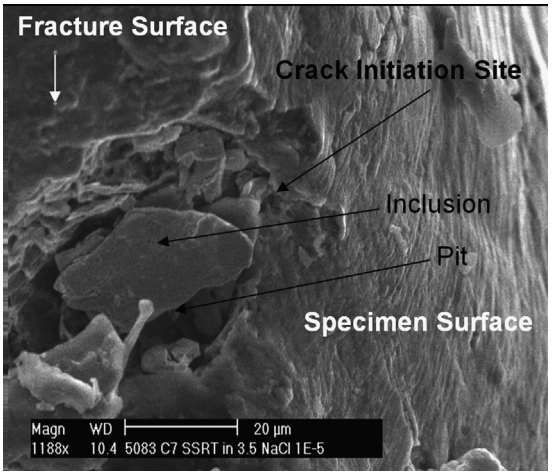

Fig. 16. SEM micrograph showing crack initiation and failure site at a cathodic pit for the conventional 5083 alloy tested at a strain rate of $E^{-5}\,s^{-1}$.

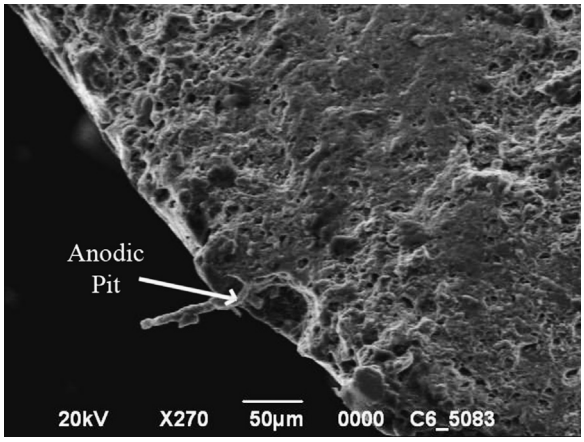

Fig. 19. SEM micrograph showing deep anodic pit failure for the conventional 5083 alloy tested at a strain rate of $1E^{-7}\,s^{-1}$.

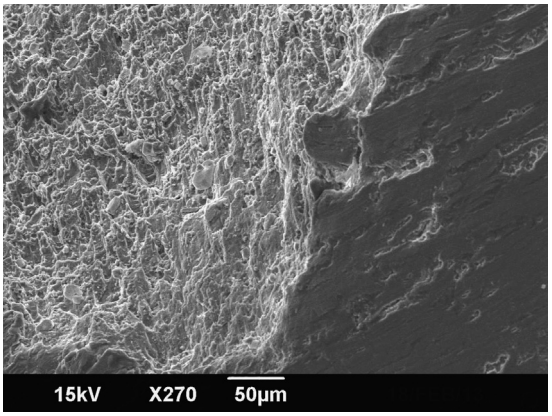

Fig. 17. SEM micrograph showing failure initiation at pits and second phase particles for the conventional 5083 alloy tested at a strain rate of $1E^{-6}\,s^{-1}$.

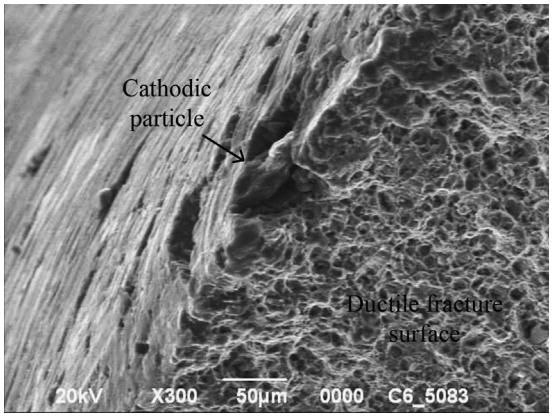

Fig. 20. SEM micrograph showing deep anodic pit failure for the conventional 5083 alloy tested at a strain rate of $1E^{-7}\,s^{-1}$.

failure. The optical micrographs for the UFG Al–7.5 Mg alloys are shown in Fig. 11(a–c). Unlike its conventional counterpart, the UFG alloy displays no visible pitting at any of the three strain rates. Instead, exfoliation, resembling fish scales, can be observed on the surface of the samples with cracks emanating from the edges and top of the scales. The cracks appear to get longer, deeper and more severe as the strain rate decreases (Fig. 12(a and b)). Exfoliation and secondary cracking are known forms of stress corrosion cracking and have shown up in this same alloy in various environments [2].

Scanning Electron Microscopy (SEM) was executed next to help elucidate the variation in mechanical behavior as well as to build on the optical results. Fig. 13(a–c) shows the progression of the pitting and cracking as a function of decreasing strain rate for the conventional 5083 alloy. At a strain rate of $1E^{-5}\,s^{-1}$, thin, fine cracks can be seen originating from tiny round pits approximately 5 μm in size. Fig. 14 shows the SEM micrograph of a pit that has formed on the surface of the conventional alloy; intergranular corrosion in the pit and secondary transgranular cracking is obvious. EDAX of the pit showed high concentration of Al and Mg within the pit, Fig. 15. Based on the previous work [1,2,17] with these specific alloys, it is believed that these are anodic pits which have formed at second phase β strengthening particles. At slower strain rates of $1E^{-6}\,s^{-1}$ and $1E^{-7}\,s^{-1}$, the SEM figures show that the pits and cracks are larger and have formed perpendicular to the extrusion direction and parallel with the machining direction. For the conventional 5083 alloy, at a strain rate of $1E^{-5}$ failure was predominately initiated at pits. Although anodic pits were noted on the specimen surface in optical microscopy, cathodic particles which promoted pit formation through dissolution of the surrounding matrix were observed as the cause of catastrophic failure (Fig. 16). At slower strain rates, the failure was initiated by a combination of anodic and cathodic pitting. Fig. 17 shows failure initiation at a line of coalesced anodic pits in a conventional alloy tested at a strain rate of $1E^{-6}$. The fracture surface shows initial transgranular crack propagation followed by ductile dimple rupture. At the slowest strain rate, very deep pits that have coalesced can be observed near the fracture surface and on the side of the specimen near failure initiation, Fig. 18. The main difference between the cause of failure initiation at strain rate of $1E^{-6}$ and $1E^{-7}$ is related to the depth of the corrosion attack. Figs. 19 and 20 show evidence of deep anodic and cathodic pits that are approximately 50 μm deep, having formed at the slowest strain rate. Large regions where corrosion attack occurred on the gage section of the sample yielded different stress corrosion responses. Fig. 21 shows an SEM of the conventional 5083 alloy at the slowest strain rate; two spots were investigated with EDAX to identify the chemical composition of corrosion attack. The first area, labeled spot#1, shows corrosion attack extending approximately 150 μm in diameter. This mud cracking appearance is the breakdown of the

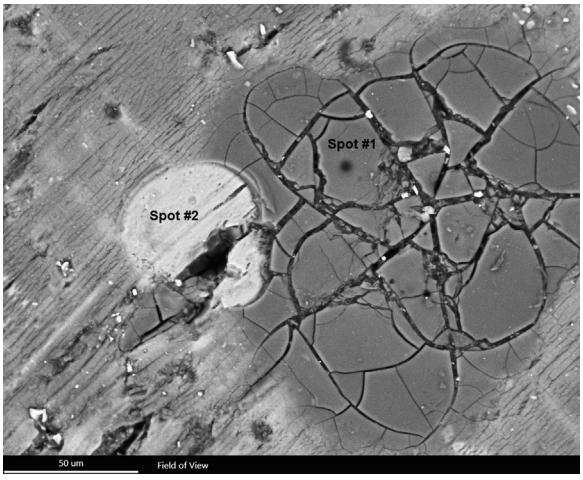

Fig. 21. SEM of the conventional 5083 alloy showing two spots that were investigated with EDAX to identify the chemical composition of corrosion attack at a strain rate of $1E^{-7}\,s^{-1}$.

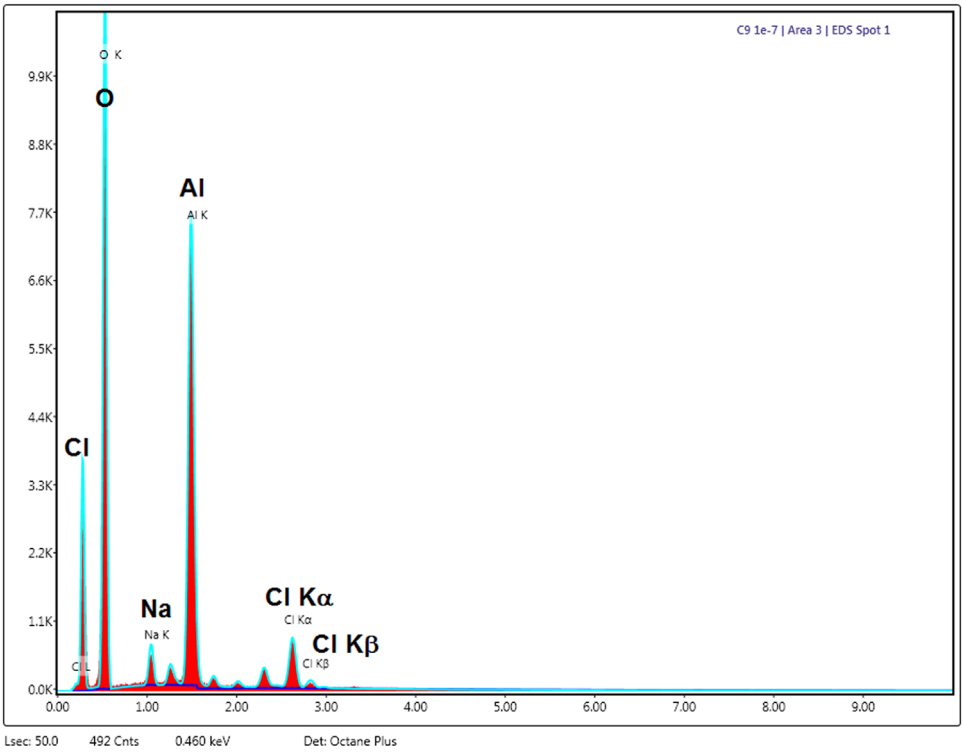

Fig. 22. EDAX pattern which identifies the chemical composition of spot#1 in Fig. 21 which includes Al, O, Cl and Na in the corrosion attack.

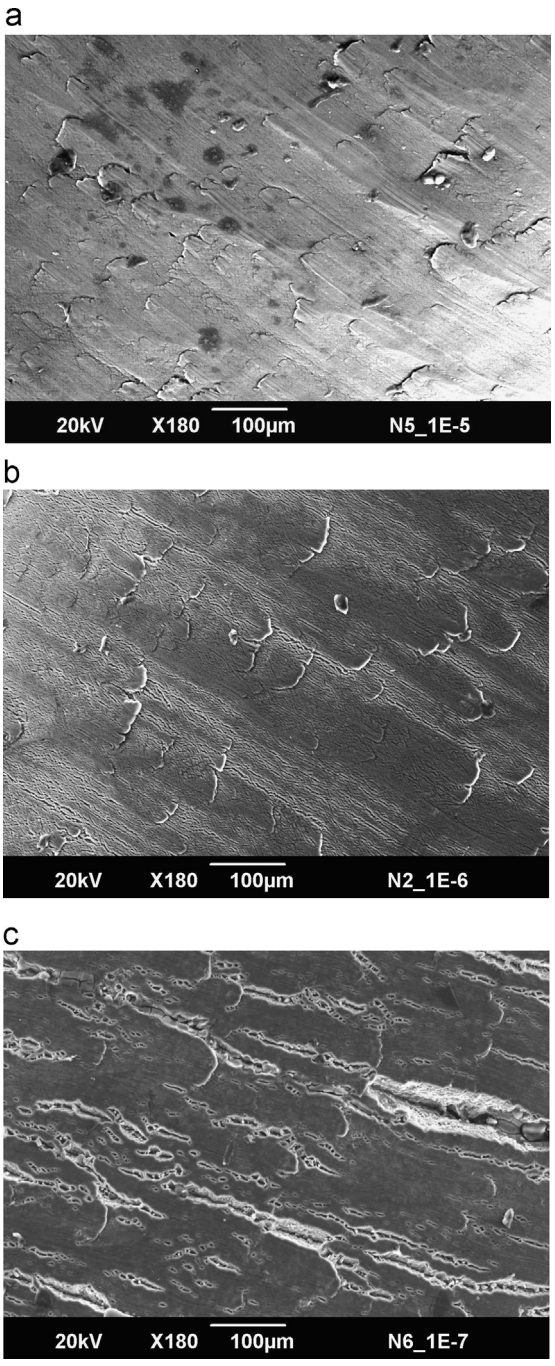

Fig. 23. SEM micrographs of UFG Al–7.5Mg alloy showing exfoliation corrosion damage as a function of strain rate: (a) $E^{-5}\,s^{-1}$, (b) $E^{-6}\,s^{-1}$, and (c) $E^{-7}\,s^{-1}$.

passive film which formed on the surface and then failed under continued stress in the natural seawater environment. Fig. 22 shows the EDAX pattern which identifies the chemical composition includes Al, O, Cl and Na.

SEM analysis of the UFG alloy revealed that in addition to the exfoliation corrosion that was obvious on the optical micrographs, extremely tiny pits in between the exfoliation scales can be seen on samples tested at a strain rate of $1E^{-6}\,s^{-1}$. Fig. 23(a–c) shows the micrographs at the three different strain rates. At a rate of $1E^{-7}s^{-1}$, the scales can be seen, but more apparent are the pits which have initiated at the edges of the exfoliation scales. Intergranular fallout is apparent as remaining particles can be seen in the deeper and wider pits, Fig. 24. Failure initiated at large inclusions which acted as stress concentrations at or near the

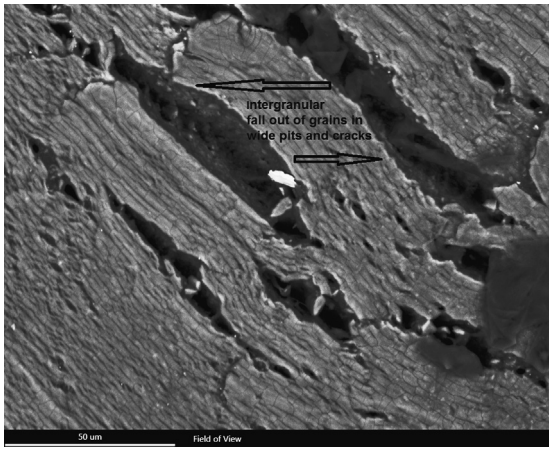

Fig. 24. SEM micrographs of UFG Al–7.5Mg alloy showing intergranular fall out in the deep cracks and pits.

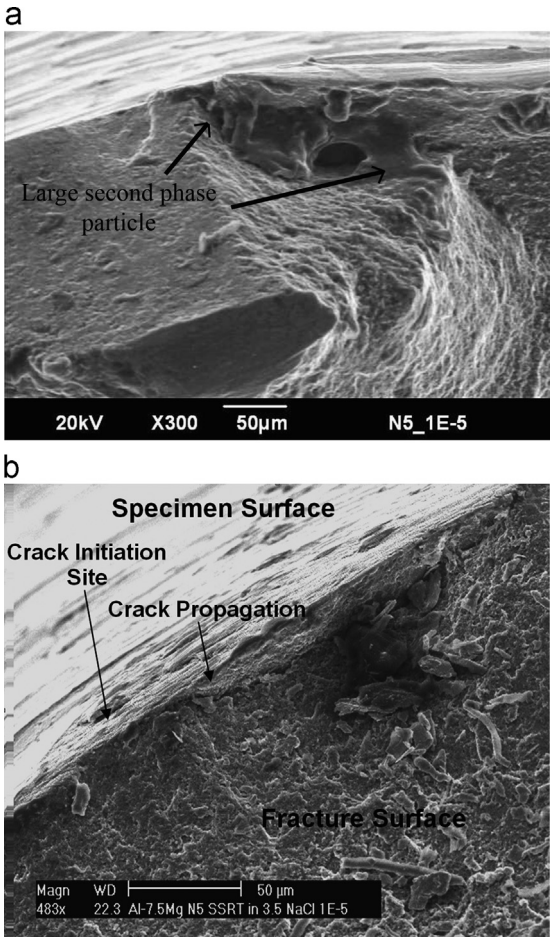

Fig. 25. SEM analysis showing crack initiation sites at a strain rate of $E^{-5}\,s^{-1}$ for the UFG Al–7.5Mg alloy at second phase inclusions which acted as stress concentrators.

surface for UFG alloys that were tested at a rate of $1E^{-5}$, Fig. 25(a and b). At the two slower strain rates, extremely fine anodic pitting and secondary cracking was clearly the cause of failure as seen in Fig. 26(a and b). The SEM micrograph of the side view of the fracture surface of the UFG alloy tested at $1E^{-6}$ reveals a columnar morphology in addition to the transgranular and ductile dimple microstructure. This columnar morphology was also noted by Han et al. [8] who investigated the strain rate ductility of cryomilled nanocrystalline Al 5083 (Al–4.2 wt% Mg–0.67 wt% Mn)

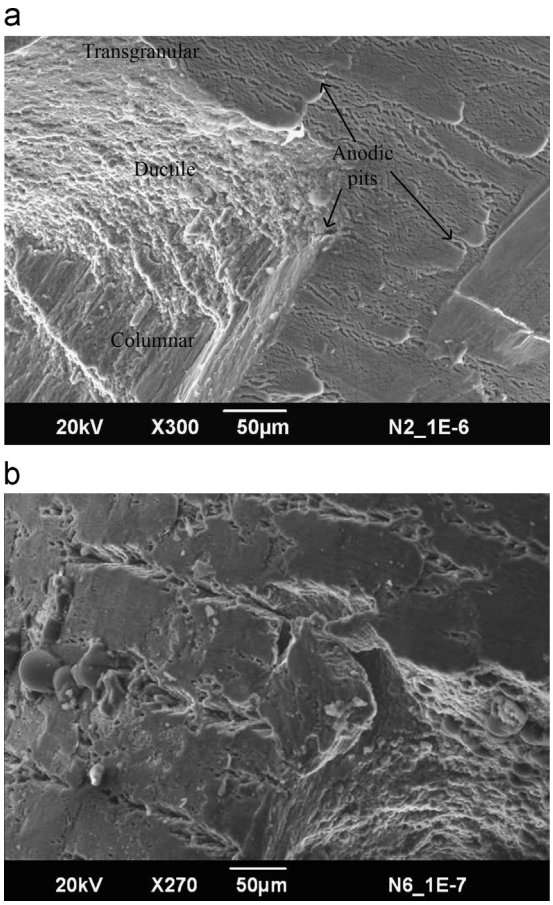

Fig. 26. SEM analysis showing crack initiation sites at fine anodic pits and secondary cracking for strain rates of (a) $E^{-6}\,s^{-1}$ and (b) $E^{-7}\,s^{-1}$ in the UFG Al–7.5Mg alloy.

in air. The researchers did not detect traditional dimple microstructure but did observe a ductile fracture normally associated with mechanically alloyed materials.

Earlier studies [40,41] have identified residual porosity and impurities to be the controlling factors in resulting mechanical properties for NC and UFG materials. These aspects usually lead to poor tensile ductility when tested in air. Fig. 5 shows that for the conventional 5083, as the strain rate decreases, UTS and YS increase slightly. Previous work has attributed this behavior to dynamic strain aging (DSA) or the Portevin–Le Chatelier [8,22–24] where the flow stress increases at a lower strain by imposing a drag force on the moving dislocations. The fast diffusing solute atoms diffuse into dislocations, thus impeding the motion and causing negative strain rate sensitivity [22]. The UFG alloy is clearly strain rate sensitive but DSA cannot be used to explain the behavior as the UTS and YS actually decrease with lower strain rate. Han et al. [8] found their nanocrystalline 5083 alloy to have negative strain rate sensitivity and attributed the behavior to DSA. A noteworthy difference between previous studies claiming DSA effect is that they have all been tested in air. In the current study, additional mechanisms due to pitting corrosion must also be considered because of the natural seawater environment. The optical and SEM micrographs support the fact that pitting/exfoliation and secondary cracking, all forms of stress corrosion, have a significant effect on the mechanical properties and can be used to explain the decreasing UTS and YS of the UFG alloy with decreasing strain rate as there is more time for corrosion attack to ensue and propagate. But this does not explain the increased ductility of the UFG Al–7.5Mg alloy with decreasing strain rate, since it would be expected that pitting and secondary cracking has a negative effect on ductility. The process of cryomilling can introduce H, C O, N, and Fe in the cryomilled powders (i) by adsorption on the surface of the metal specimen, (ii) as an impurity atom within the lattice, and/or (iii) through the yielding of second phases [8,28,29,42,43]. The EDAX results in Fig. 27 reveal that impurity elements O, C and Fe were identified in the UFG

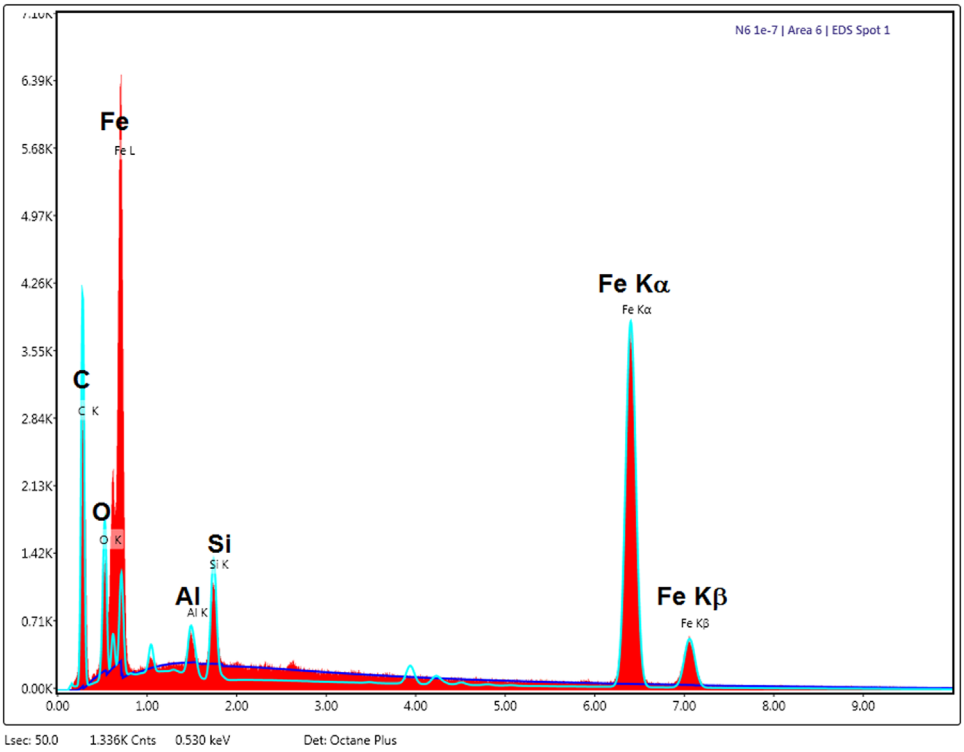

Fig. 27. EDAX results that identify impurity elements O, C and Fe are in the UFG 7.5Al alloys.

alloys. Han et al. [8] believed that in practice, the diffusion of these atoms into dislocations through the DSA mechanism would actually retard the movement of the dislocation, thus promoting crack initiation with a higher flow stress. Consequently, they proposed a separate diffusion-mediated stress relaxation mechanism is responsible for the enhanced ductility in their nanocrystalline 5083 at lower strain rates. The diffusion-mediated stress relaxation mechanism differs from the DSA mechanism as it relates to stationary stress concentration sites as opposed to moving dislocations. Under loading, it is expected that cracks will initiate at inhomogeneities which may include defects, impurities, interfaces, grain boundaries and corrosion pits. These discontinuities create localized stress concentrations much higher than the applied stress. Han et al. [8] justified their theory of diffusion-mediated stress relaxation using the subsequent rationale. Lower strain rates permit fast diffusing interstitial solute atoms to fill above stated defect areas. In doing so, they promote relaxation of the local stress, thereby preventing the critical stress level for crack initiation to be reached. Sites which act as pre-cursors for crack initiation will be filled with solute atoms due to the high density of dislocations promoting diffusion. The initiation and growth of resulting failure causing micro-cracks can then be significantly repressed if the strain rate is adequately low. It is believed that this mechanism is present in the UFG Al–7.5Mg alloys and can be used to help explain the enhanced ductility but corresponding decrease in UTS and YS with decreasing strain rate, contradicting the results found by Han et al. [8] and their cryomilled Al 5083. Although the fast diffusing impurities and high dislocation density help to relieve stress concentration and prevent crack initiation, anodic pitting and intergranular fall out introduce sites for potential crack initiation, thus decreasing strength while maintaining a high elongation. Cheng et al. [25], who investigated ball-milled copper, observed a similar trend of higher ductility and lower UTS at lower strain rate. They witnessed nearly perfectly plastic behavior in their copper materials as the strain rate decreased from $10^{-2}\,s^{-1}$ to $10^{-4}\,s^{-1}$ while the elongation doubled from 5.1% to 11.1%. Their contradiction in property trends from Han et al. [8] and their cryomilled Al 5083 was attributed to manufacturing consequences. Ball milling normally introduces a significant amount of defects that lead to crack sites but was balanced by the introduction of fast diffusing impurities such as O, N, C and H, and high dislocation density, that work to relieve stress concentrations, thereby delaying crack initiation.

The proposed mechanisms of diffusion-mediated stress relaxation and advanced pit propagation and secondary crack propagation can explain the increased ductility and decreased strength of the UFG Al–7.5Mg alloy as a function of decreasing strain rate. However, more experimental studies as a function of environment are needed to substantiate the validity of these claims.

5. Conclusion

The wrought conventional 5083 H-111 alloy displayed negative strain rate sensitivity in a natural seawater environment which was explained by dynamic strain aging and the Portevin–Le Chatelier (PLC) effect. UFG Al–7.5Mg alloy produced by cryomilling and subsequent hot extrusion displayed higher ductility, lower tensile and yield strength at lower strain rates. The higher ductility was explained by a new mechanism, diffusion-mediated stress relaxation, while the reduction in strength was attributed to deep anodic corrosion pits. Based on the experimental results of this and previous related studies, it appears that the UFG Al–7.5Mg alloy has better resistance to pit initiation than the conventional 5083 alloy, under constant strain. Both materials displayed evidence of stress corrosion cracking during testing in dissimilar ways. Results show that the conventional 5083 is less affected by strain rate in a marine environment than the UFG Al–7.5Mg material. As strain rate decreased, pit propagation was a concern for the UFG Al–7.5Mg alloy. These differences are attributed to material composition, grain size, number and distribution of second phase particles, impurities and inclusions as a result of differences in manufacturing processes.

Acknowledgments

This work was sponsored by the NACE International Seed Grant # #N000140210024.

The authors would also like to thank The LaQue Testing and Research Center for their assistance in testing and analysis. The authors also wish to acknowledge Boeing Corporation and Enrique Lavernia at UC Irvine for providing the nanostructured alloys.

References

[1] E. Sikora, X. Wei, B. Shaw, Corros. Sci. 60 (2004) 387–398.
[2] M.M. Sharma, C.W. Ziemian, J. Mater. Eng. Perform. 17 (2008) 870–878.
[3] J.C. Chang, T.H. Chuang, Metall. Mater. Trans. A 30A (1999) 3192.
[4] N. Winzer, A. Atrens, W. Dietzel, V.S. Raja, G. Songe, K.U. Kainer, Mater. Sci. Eng. A 488 (2008) 339–351.
[5] N.J. Petch, J. Iron Steel Inst. 23 (1953) 25–28.
[6] R. Schwaiger, B. Moser, M. Dao, N. Chollacoop, S. Suresh, Acta Mater. 51 (2003) 5159.
[7] Q. Wei, S. Cheng, K.T. Ramesh, E. Ma, Mater. Sci. Eng. A 381 (2004) 71.
[8] B.Q. Han, J.Y. Huang, Y.T. Zhu, E.J. Lavernia, Scr. Mater. 54 (2006) 1175.
[9] Y.M. Wang, A.M. Hodge, P.M. Bythrow, T.W. Barbee Jr., A.V. Hamza, Appl. Phys. Lett. 89 (2006) 081903.
[10] A.P. Zhilyaev, T.G. Langdon, Prog. Mater. Sci. 53 (2008) 893–979.
[11] R.Z. Valiev, T.G. Langdon, Prog. Mater. Sci. 51 (2006) 881–981.
[12] N. Gao, C.T. Wang, R.J.K. Wood, T.G. Langdon, J. Mater. Sci. 47 (2012) 4779–4797.
[13] B. Ahn, R. Mitra, A.M. Hodge, E.J. Lavernia, S.R. Nutt, Mater. Sci. Forum 584–586 (2008) 221–226.
[14] Ramana M. Pidaparti, Appajoysula S. Rao, Corros. Sci. 50 (2008) 1932–1938.
[15] Yongfang Huanga, Cheng Weib, Lijie Chena, Peifeng Lic, Eng. Fail. Anal. 44 (2014) 168–178.
[16] G.R. Argade, N. Kumar, R.S. Mishra, Mater. Sci. Eng. A 565 (2013) 80–89.
[17] Mala M. Sharma, Josh D. Tomedi, Jeffery M. Parks, Corros. Sci (2014) (submitted for publication).
[18] J.L. Searles, P.I. Gouma, R.G. Buchheit, Metall. Mater. Trans. A 32A (2001) 2859.
[19] B.Q. Han, J.Y. Huang, Y.T. Zhu, E.J. Lavernia, Acta. Mater. 54 (2006) 3015–3024.
[20] Andrew C. Magee, Leila Ladani, Mater. Sci. Eng. A 582 (2013) 276–283.
[21] Mingliang Wang, Aidang Shan, J. Alloys Compd. 455 (2008) L10–L14.
[22] J. Balik, P. Lukac, Acta. Metall. Mater. 41 (1993) 1447.
[23] M. Wagenhofer, M. Erickson-Natishan, R.W. Armstrong, F.J. Zerilli, Scr. Mater. 41 (1999) 1177.
[24] A.H. Clausen, T. Borvik, O.S. Hopperstad, A. Benallal, Mater. Sci. Eng. A 364 (2004) 260.
[25] S. Cheng, E. Ma, Y.M. Wang, L.J. Kecskes, K.M. Youssef, C.C. Koch, et al., Acta. Mater. 53 (2005) 1521.
[26] M.C. Carroll, P.I. Gouma, M.J. Mills, G.S. Daehn, B.R. Dunbar, Scr. Mater. 42 (2000) 335.
[27] G. Lucadamo, N.Y.C. Yang, C. San Marchi, E.J. Lavernia, Proceedings of MRS Symposium, vol. 882E, 2005, EE5.2.1.
[28] V.L. Tellkamp, A. Melmed, E.J. Lavernia, Metall. Mater. Trans. A 32A (2001) 2335.
[29] F. Zhou, J. Lee, S. Dallek, E.J. Lavernia, J. Mater. Res. 16 (2001) 3451.
[30] F. Le Chatelier, Rev. de Métall. 6 (1909) 914.
[31] A. Portevin, F. Le Chatelier, C. R. Acad. Sci. Paris 176 (1923) 507.
[32] S.L. Mannan, Mater. Sci. 16 (6) (1993) 561–582.
[33] P. Rodriguez, Bull. Mater. Sci 6 (4) (1984) 653–663.
[34] H. Dierke, et al., Comput. Mater. Sci. 39 (2007) 106–112.
[35] M. Abbadi, P. Hähner, A. Zeghloul, Mater. Sci. Eng. A 337 (2002) 294.
[36] F.B. Klose, A. Ziegenbein, F. Hagemann, H. Neuhäuser, P. Hähner, M. Abbadi, A. Zeghloul, Mater. Sci. Eng. A 369 (2004) 76.
[37] Y. Estrin, M.A. Lebyodkin, Mater. Sci. Eng. A 387–389 (2004) 195.
[38] Győző Horváth, Nguyen Q. Chinh, Jenő Gubicza, János Lendvai, Mater. Sci. Eng. A 445–446 (2007) 186–192.
[39] S.S. Woo, Y.R. Kim, D.H. Shin, W.J. Kim, Scr. Mater. 37 (1997) 1351–1358.
[40] P.G. Sanders, J.A. Eastman, J.R. Weertman, Acta Mater. 45 (1997) 4019.
[41] P.G. Sanders, G.E. Fougere, L.J. Thompson, J.A. Eastman, J.R. Weertman, Nanostruct. Mater. 8 (1997) 243.
[42] Kyung H. Chung, Enrique J. Lavernia, Metall. Mater. Trans. A 33A (2002) 3795.
[43] B.Q. Han, E.J. Lavernia, F.A. Mohamed, Metall. Mater. Trans. A 36A (2005) 345.